Pterodactyl: Aerodynamic and Aerothermal Modeling for a Symmetric Deployable Earth Entry Vehicle with Flaps

Brandon J. Reddish[1]
University of California Davis, Davis, CA, 95613, USA

Ben E. Nikaido[2], Sarah N. D'Souza[2]
NASA Ames Research Center, Moffett Field, CA, 94035, USA

Veronica M. Hawke[3], Zane B. Hays[4]
Science and Technology Corp., Moffett Field, CA, 94035, USA

Hyung Suk Kang [5]
John Hopkins University Applied Physics Laboratory, Laurel, MD, 20723, USA

Abstract

NASA's Pterodactyl project has investigated a deployable atmospheric entry vehicle integrated with a flap control system that provides precision targeting during reentry. The control system consists of eight flaps mounted at the edge of a heatshield that can deflect in and out of the flow. An aerodynamic and aerothermodynamic analysis process was developed for preliminary vehicle design and aerodynamic database generation using engineering and CFD tools with varying levels of fidelity. The objective of this analysis was to: 1) understand the inherent aerodynamics, 2) provide an aerodynamics database for stability and control analysis, and 3) provide qualitative and quantitative aeroheating analysis for Thermal Protection System modeling of the flaps. A high fidelity Euler code, Cart3D, was used to resolve complex flow features such as secondary shocks and shock impingement. A wide range of supersonic (Mach 2) and hypersonic Mach numbers (up to Mach 40) were tested with an Earth atmosphere model. A process was developed to utilize the adaptive volume mesh generator utility of the perfect gas model of Cart3D to create meshes with high cell efficiency and numerical stability prior to running a 2nd order accurate solution with a real gas model. High-fidelity aerothermal CFD simulations were performed using US3D to further improve the aerothermal analysis on hypersonic flow around a complex entry vehicle shape including viscosity, chemical reactions of air species, vibrational energy, and catalytic surface reactions. In this process, it was found that the flap control system provided multi-axis control that can be utilized for entry precision targeting. Addtionally, the Pterodactyl vehicle can achieve up to a trim L/D of 0.2. Finally, the increased fidelity of the aerothermal heating environments revealed that the shear stress contributes to increasing the heating on the flaps.

[1] Graduate Student, Department of Mechanical and Aerospace Engineering, UC Davis
[2] Aerospace Flight Systems Engineer, Systems Analysis Office, NASA/ARC, AIAA Member.
[3] Senior Research Scientist, Systems Analysis Office, AIAA Member.
[4] Aerospace Engineer, Analytical Mechanics Associates, Inc.
[5] Aerodynamic Engineer, Air and Missile Defense Sector

I. Nomenclature

α	=	angle of attack
β	=	sideslip angle
δ	=	flap deflection angle
L/D	=	lift-to-drag ratio
p	=	Pressure (Pa)
t	=	Translational temperature (K)
tv	=	Vibrational temperature (K)
T	=	metric ton
Qw	=	Surface heat flux (W/m^2)
τ_w	=	Wall shear stress (Pa)
$\lvert\tau_{wx}\rvert$	=	Magnitude of wall shear stress in *x*-direction (Pa)
$\lvert\tau_{wy}\rvert$	=	Magnitude of wall shear stress in *y*-direction (Pa)
$\lvert\tau_{wz}\rvert$	=	Magnitude of wall shear stress in *z*-direction (Pa)
x	=	Streamwise direction in CFD coordinate (see Figure 4 and Figure 9)
y	=	Vertical direction from coordinate origin to top (see Figure 4 and Figure 9)
z	=	Spanwise direction normal to symmetry plane (see Figure 4 and Figure 9)
MRC	=	moment reference center
LE	=	leading edge
TE	=	trailing edge
CP	=	center of pressure

II. Introduction

The Pterodactyl project investigates the design of a unique entry vehicle configuration with a novel control system that provides the capability of precision landing. A Deployable Entry Vehicle (DEV) has the capability of folding a flexible aeroshell into a smaller form factor during launch which later expands to a blunt body shape for entry to generate a larger ballistic coefficient. An example of a DEV in a stowed and deployed configuration is displayed in Figure 1.

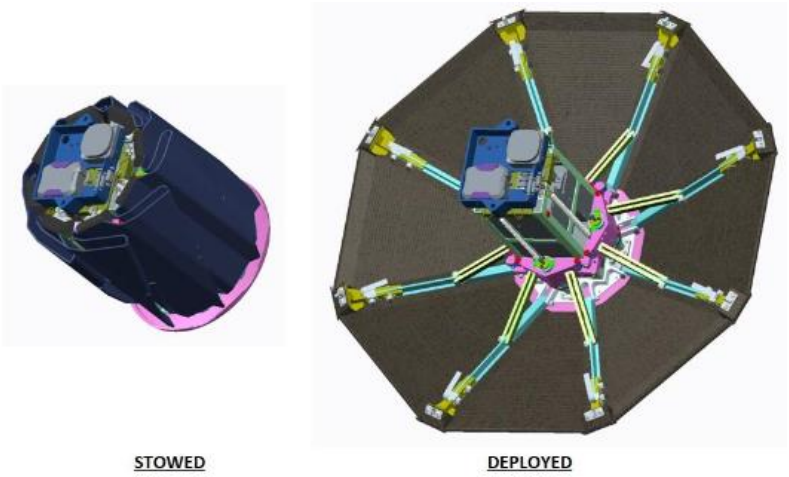

Figure 1 Deployable entry vehicle in stowed and deployed configuration[1]

The need for large mass payloads (≥ 2 T) has grown for future space missions, but the size of rigid aeroshells to deliver such payloads has grown beyond the stowed diameter constraints of current launch systems.[2] The DEV design offers an alternative to the rigid aeroshell with more efficient packing and adequate thermal protection during entry. The DEV concept has been tested with an application to cube satellites with the Adaptive Deployable Entry and Placement Technology (ADEPT) project[1] The ADEPT system can deliver the same science payload with a stowed diameter 3-4 times smaller than an equivalent rigid aeroshell. The ADEPT design uses an umbrella-like deployable structure with a 3-D woven carbon fabric that makes up most of the thermal protection system (TPS). A flight test of

the ADEPT configuration was conducted with a sub-orbital sounding rocket at the White Sands Missile Range. During the descent, the vehicle reached a peak Mach number of three[3] and demonstrated the mechanical and system level feasibility of the design. Although the DEV design offers a solution for packaging of aeroshells, the traditional guidance and control systems implemented on rigid aeroshells do not directly translate.

The ADEPT design differs from a rigid aeroshell in that it does not have a back shell, which is where the traditional reaction control system (RCS) is located. Historically, RCS has been used as the main method of controlling blunt bodies by using small thrusters located far from the center of mass to rotate the vehicle.[4] Without a backshell, implementing RCS on the aft section of a vehicle based on the ADPET design could result in an insufficient amount of control authority. In addition to a loss of controllability, implementing RCS without a backshell could interact negatively with the payload by introducing high temperatures or damaging chemicals. The possible problems with traditional RCS inspire the development of a new way to integrate RCS or an entirely new control system for ADEPT vehicles. NASA's Pterodactyl project has been addressing the challenges associated with new guidance and control (G&C) systems for DEVs that provide the capability for precision targeting. The Pterodactyl project conducted a trade study of three different entry G&C methods for a lunar return entry vehicle with an Earth entry speed of 11 km/s.[5] The three methods included RCS, mass movement control system (MMCS), and a flap control system (FCS). Although RCS and MMCS were explored as potential control systems, FCS was chosen as the main method of control for the current phase of the Pterodactyl project. The FCS method utilizes radially mounted aerodynamic control surfaces on the Pterodactyl Base Vehicle (PBV), a 1+m diameter, asymmetric variant of ADEPT DEV, to produce the moments and forces required for controlling the vehicle orientation during flight. There were two key findings, specific to the FCS, that drive the work pursued in this paper. First, in Nikaido et al.[6], it was found that aerodynamic flap effectiveness was underpredicted when modeled with Modified Newtonian engineering methods. The pitching moment of a single flap could be off by as much as 50% at large, positive deflection angles. Second, the aeroheating study showed that at lunar return speeds, the heat rate on the aeroshell carbon fiber fabric was within the 250 W/cm^2 constraint,[1] but the localized heat rate on the edge of some flaps reached as high as 450 W/cm^2. The heating of the flap's edge occurs due to the local angle of attack of the flaps that can occur when the vehicle is at a relatively high angle of attack. Edges with relatively small radii in hypersonic flows experience greater heating than blunt shapes. Additionally, shock interactions were observed on the surfaces of the flaps which generate large amounts of heat. These two phenomena stress the importance of quality aerodynamic and aerothermodynamic databases to inform flap controller and thermal protection system (TPS) design. Based on these findings, advancements to Nikaido et al.'s methodology for modeling the complex hypersonic and supersonic flow around the Pterodactyl vehicle have been implemented for a new instantiation of the PBV, called PBV-II, which is a symmetric aeroshell scaled up to 2.86 m (Figure 2).

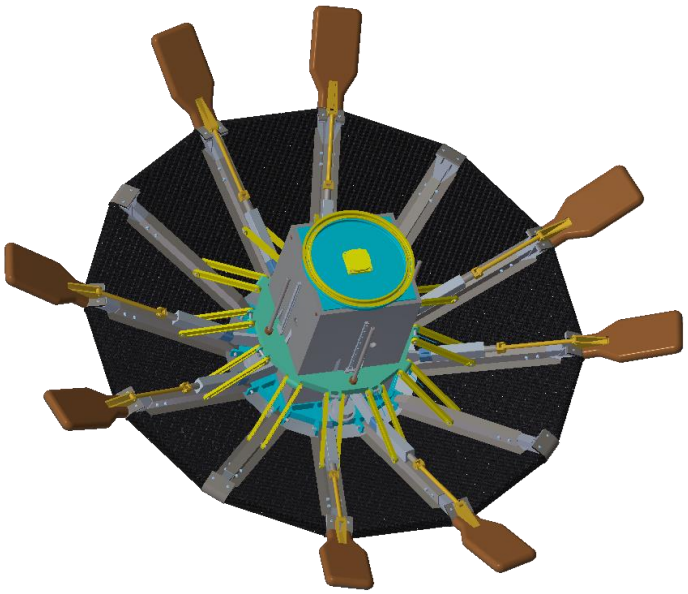

Figure 2 Pterodactyl vehicle with flaps

Nikaido et al's method utilized the efficient aerodynamic modeling tools of CBAero and Cart3D. CBAero uses a modified Newtonian method with a triangular surface mesh that is set on the outer mold line of the vehicle.[7] Cart3D solves the inviscid Euler equations and can adequately capture the majority of the complex shock phenomena that occur around a vehicle at supersonic and hypersonic speeds.[8] Both CBAero and Cart3D were used as the primary aerodynamic and aerothermal modeling tools to generate the database described in this paper. Higher fidelity simulations were needed to address the above concerns, and this was gained through inclusion of more detailed geometry, implementation of adaptive meshing, and anchoring CBAero heating to improved Cart3D. Specifically, this paper discusses how the overall process and methodology was improved upon. The following sections describe the geometry and simplifications used for modeling, Cart3D simulation mesh automation and simulation setup, anchoring of CBAero data to higher fidelity solutions, and US3D Navier-Stokes simulation set up.

III. Aerodynamic and Aeroheating Simulation Methodology

The modeling tools CBAero and Cart3D were used for the generation of the aerodynamic and aerothermal databases that feed into the design of G&C algorithms and TPS design. A previous iteration of the Pterodactyl project demonstrated the ability of both codes to generate a large aerodynamic database for prototype vehicles within a week given sufficient super computing resources.[6] CBAero uses a modified Newtonian method that calculates the flow conditions based on the Mach number and the relative angle of attack of any surface of the vehicle.[9] While this method provides aerodynamic and aerothermal predictions with great speed and computational efficiency, it cannot resolve more complex features of hypersonic flow such as oblique shocks, expansion fans, or wake flow. CBAero was used to produce preliminary estimations of aerothermal heating and aerodynamic loading. Using the CBAero data as a baseline, Cart3D was then used to generate an aerodynamic database by solving the inviscid Euler equations.[8] At the writing of this paper, the team was in the process of using the Cart3D simulation to anchor the CBAero aerothermal database. The results of that analysis will be discussed in a future paper. A full Navier-Stokes CFD solution using US3D was used to produce the highest fidelity model for a single flight condition and vehicle attitude and develop insights into differences between the varying model fidelities. An overview of the aerodynamic and aerothermal database generation process is shown in Figure 3.

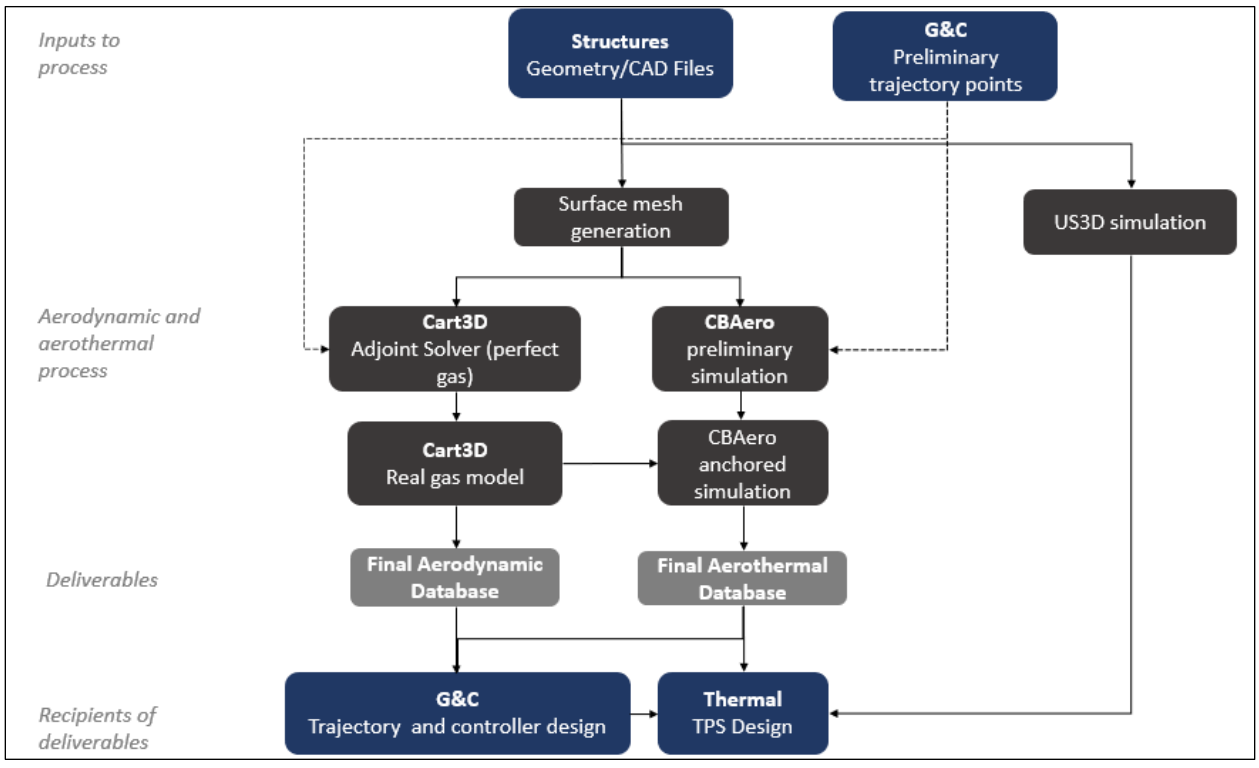

Figure 3 Aerodynamic and aerothermal database generation process for the Pterodactyl Vehicle

A. Vehicle Configuration, Flight Conditions, and Vehicle Attitude Parameters

The geometry used for the simulation was a watertight and simplified version of the Pterodactyl vehicle that is displayed in Figure 4. The geometry includes an aeroshell with a nose cap that steps down to the 3D carbon fiber fabric that is supported by metal ribs. The ribs attach in the center to a boxlike structure that represents the payload. The moment reference center is located in front of the vehicle at an offset of -0.25 meters in the *x* direction from the geometric origin determined in the Computer Aided Design (CAD) software as the center front point of the nose cap. There are eight flaps located on the edge of the vehicle as shown in Figure 5a which are numbered according to the labels in the figure. The flaps are actuated around a hinge line, just inboard of the aeroshell shoulder, and can deflect in and out of the flow to alter the induced pitching moment. The undeflected position, a deflection of 0°, is defined as being aligned with the surface of the deployed aeroshell. A positive deflection is defined as rotating into the flow and the opposite is considered a negative deflection. Figure 5b illustrates how flap deflection angle is defined.

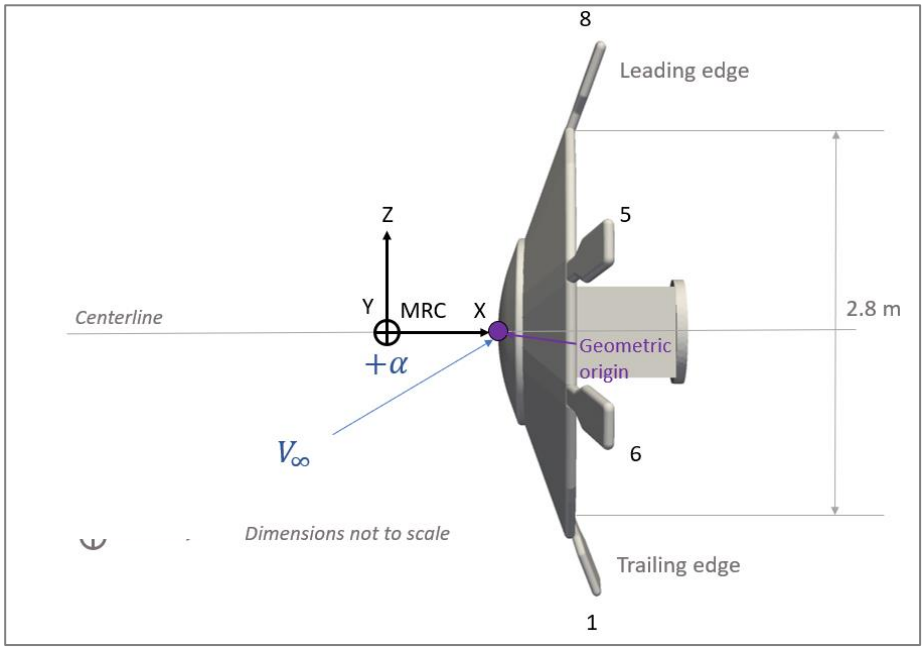

Figure 4 Pterodactyl vehicle coordinate system and dimensions

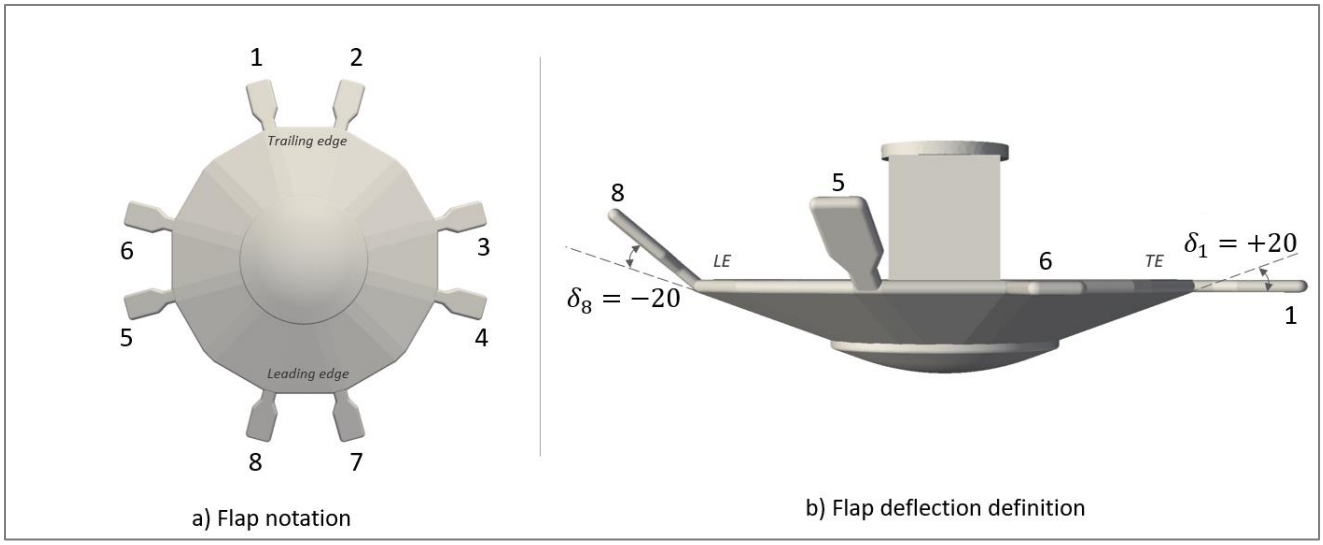

Figure 5 Pterodactyl vehicle flap labeling and deflection orientation

The CFD simulation matrix was chosen using a reference lunar return Earth entry trajectory.[6] The run cases are made of all combinations of the values presented in Table 1. The CBAero matrix is broken into two sections, one consisting of a limited matrix for preliminary aerodynamic results and another matrix for the aerothermal analysis that uses the results from the Cart3D aerodynamic database. For a given geometry, all flaps are deflected at the same angle at each (Mach, α, β) condition. The work done in reference 6 showed that there is a negligable amount of interaction between the flaps, which allows for all flaps to be deflected at the same angle during the simulation, seperated by component during post-processing, and recombined to produce any unique combination of independently deflected flaps with the PBV. The following sections describe the justification and implementation of the aerodynamic and aerothermal processes used for this research.

Table 1 Aerodynamic database CBAero and Cart3D simulation matrix.

Method		Angle of attack (α) [deg]	Sideslip (β) [deg]	Mach	Flap Deflection [deg]
CART3D		-20, -15, -10, -5, 0	0, 5, 10, 15, 20	2, 5, 10, 15, 20, 31, 40	-45, -20, 0,10, 20, 30
CBAERO (Anchored aerothermal)	Set1	-20, -15, -10, -5, 0	0, 5, 10, 15, 20	2, 5, 10, 15, 20, 31, 40	-45, -20, 0, 10, 20, 30
	Set2	-5, -10, 0, 5, 10	0, -5, -10	5, 10, 15, 20, 31, 40	-45, -20, 0, 10, 20

B. Cart3D Simulation Setup

Aerodynamic Database Setup

Cart3D was chosen for the purposes of producing an accurate database for the prototype development of the Pterodactyl vehicle. This simulation package solves the inviscid Euler equations with a finite volume, cell-centered, second order accurate upwind scheme with a weak imposition of boundary conditions.[10][11] At supersonic and hypersonic speeds, the forces and moments experienced by blunt bodies are influenced by inviscid flow features more than viscous shear forces. The main source of these forces comes from the bow shock that occurs in front of the blunt body. The Euler equations can resolve such features. Additionally, this study used a version of Cart3D that uses an equilibrium gas model to better model the gas chemistry of the air as it reaches high temperatures that alter the ratio of specific heats. Real gas chemistry greatly influences the behavior of secondary shock features around the flaps and expansion fans near the nose cap and shoulder of the heat shield. The influence of normal pressure forces on the vehicle verses viscous shear forces is greatest at higher Mach numbers for blunt bodies. Because of this relationship, there is greater confidence in the solutions at hypersonic speeds (> Mach 5) than the supersonic cases. Without experimental validation data, the quality of the results can only be assessed in terms of numerical accuracy and convergence, and prior validation with similar re/entry flows.

Meshing Procedure

The computational efficiency of the unstructured Cartesian mesh utilized in Cart3D allowed for the production of highly refined volume meshes that covered a wide range of flight conditions without a large number of person-hours dedicated to optimizing the grid and minimizing the number of cells used. The meshing procedure outlined in reference 6 used a general volume mesh that could be used for different flight conditions but had a low cell efficiency. To improve the stability of the solution and reduce the total number of volume cells, a pseudo back body was added to the geometry of the vehicle. The surface pressures that drive the forces and moments on the vehicle are predominately located on the windward side due to the high speeds and the blunt body shape of the vehicle. Because of this, the forces acting on the pseudo back shell were ignored in the summation of forces and moments. In addition to the pseudo back shell, the flow domain aft of the vehicle extends less than half a diameter of the heatshield diameter. With supersonic and hypersonic flow, information cannot travel upstream and will not affect the overall flow characteristics on the high-pressure regions of the flow. The complex flow behind the heatshield has little influence on the total loads acting on the vehicle, however without a back shell, the simulations provide no information on any dangers that the flow environment may pose to the exposed payload. The inviscid Euler equations are not adequate to resolve the turbulent and separated flow in the aft region of the vehicle, so the placement of the pseudo back shell does not limit the modeling capability of Cart3D. The pseudo back shell and cut-plane of the pre-specified volume mesh are displayed in Figure 6. This method showed adequate levels of both iterative and mesh convergence and produced runs that took approximately 30 minutes to complete per case.[6]

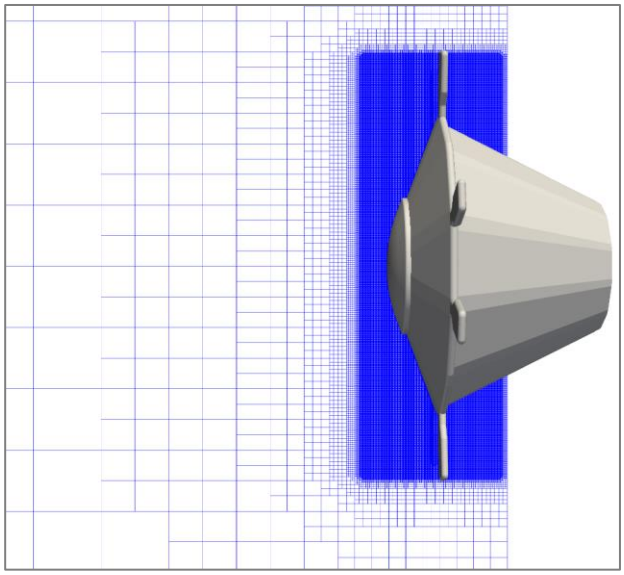

Figure 6 Pre-specified volume mesh cut-plane and simplified geometry with pseudo back shell

Another alternative meshing method was also investigated with the goal of reducing the size and improving the quality of the mesh such that the solution times are the same or less than the pre-spec method, in addition to producing a more refined solution. Specifically, the Cart3D adjoint-based adaptive mesh refinement tool, with a mesh-adaptation strategy designed to minimize the cost of the simulation[12], was used. The first step in this process was to develop a surface mesh that is refined around the more complex surfaces of the vehicle, such as the shoulder of the heat shield, the flaps, and the nose cap. Because the adjoint solver could improve the stability of the simulation while reducing the total volume cells, the two techniques of adding a pseudo back shell and shortening the domain aft of the vehicle were not implemented for this method. Once generated, the surface mesh is fed into the Cart3D perfect gas solver using an estimated value for gamma (the ratio of specific heats) to get close to the shock standoff distance. For the Mach number of 2.5, a gamma value of 1.4 was used, and for the hypersonic cases of Mach 5 and greater, a gamma value of 1.3 was used. Adjusting this number for the perfect gas model allows the adjoint meshing algorithm to better predict the location of the different shock features. A buffer parameter was set in the adjoint solver that created larger regions of high cell density around the bow shock to account for the small error in the estimation of gamma. The adjoint solver conducted seven cycles of refinement based on the converged solution of the previously simulated volume mesh. This final mesh was then solved with the real gas version of Cart3D. An example of a mesh at the final level of refinement is shown in Figure 7.

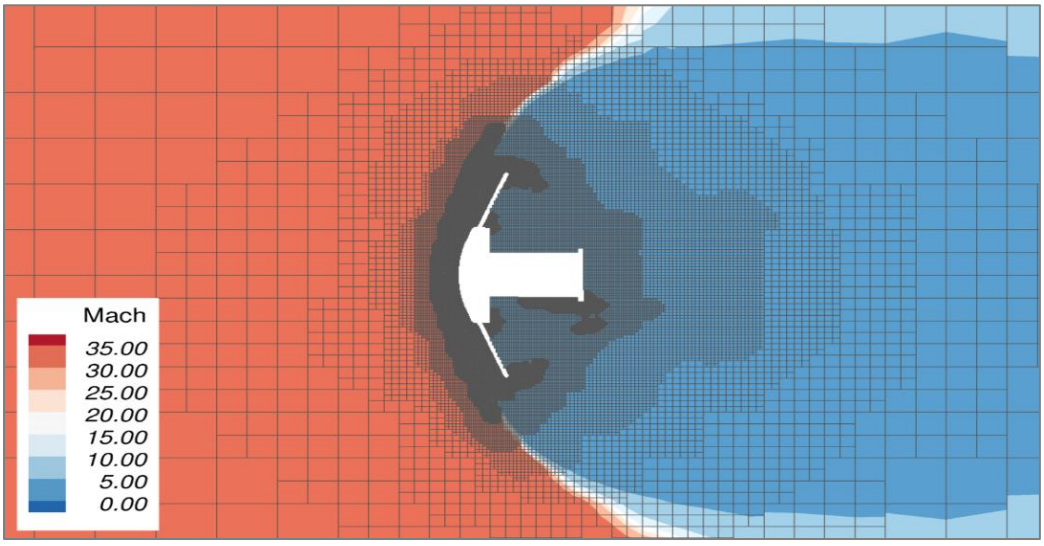

Figure 7 Cut plane of flow field and volume mesh at Y=0

Investigation of these meshing options showed that implementation of the adjoint method matched or exceeded the performance of the pre-specified method after approximately 30 minutes of 'real-time' computation required per simulation. The pre-specified method generated a volume mesh with an average of 350 million cells, and the adjoint method produced meshes with an average of 7 million cells. Additionally, investigations found that the additional time spent on each case in the meshing phase for the adjoint method allowed for faster solutions with increased accuracy. Therefore, the results reported in this paper will be from use of the Cart3D adjoint-based adaptive mesh refinement tool.

C. Database Symmetrization

Due to inherent numerical error and possible unsteadiness in CFD simulations, the aerodynamic database was symmetrized to generate an idealized model of the vehicle flight characteristics for use in the design of the controller for the flaps. The PBV-II is aerodynamically symmetric about the xy- and xz-planes allowing for the reduction of the required Cart3D simulations. Positive α and β conditions were reflected across the y and z-planes to fill out the database and ensure force and moment symmetry for the aeroshell as well as the flaps. Table 2 shows the correlation between the forces and moments of a pure angle of attack condition to those of a pure sideslip angle. The values of C_{mx} (the moment about the x-axis) are not represented because for a pure angle of attack (no sideslip), there is no rolling moment due to the symmetry of the vehicle.

Table 2 Body force and moment symmetry mapping for pure angle of attack and pure sideslip.

Pure Angle of Attack Force or Moment ($\beta = 0$)	Pure Sideslip Angle Force or Moment ($\alpha = 0$)
$+C_L$	$-C_S$
$+C_D$	$+C_D$
$+C_S$	$-C_L$
$+C_{my}$	$-C_{mz}$
$+C_{mz}$	$-C_{my}$

Since this process treats the geometry as a collection of separate regions, the aeroshell and each flap, the flaps were also symmetrized to provide the best model for control design. The flaps act independently of each other but have unique attitudes relative to the freestream flow. Figure 8 shows the magnitude correlation between flaps at a pure angle of attack and pure sideslip. The colors correlate the equivalent magnitude values for the flaps at a pure angle of attack flight condition on Figure 8a and a pure sideslip flight condition on Figure 8b.

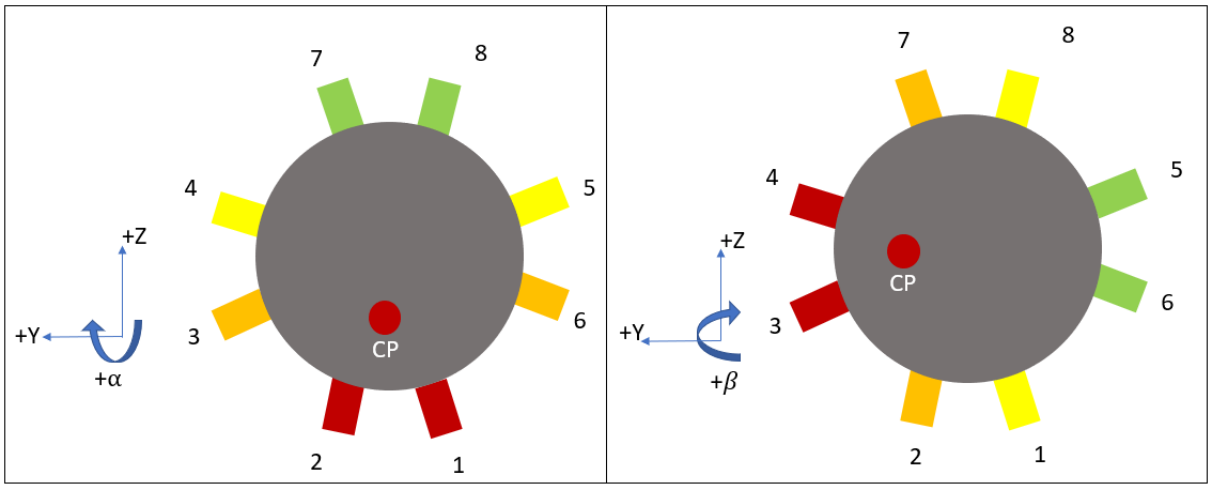

(a) Pure angle of attack (b) Pure sideslip

Figure 8 Flap aerodynamic similarity for a general angle of attack and corresponding sideslip angle

Figure 8 illustrates that for an angle of attack of 5° the magnitude of forces and moments of flap 1 should ideally match the forces and moments experienced by flap 3 at a sideslip angle of 5°. The symmetrization process was applied only to the cases where either angle of attack is zero or sideslip angle is zero. This section of data points does not include the majority of points that have non-zero values for both angle of attack and sideslip angle. The symmetry rules applied to this select region and was sufficient to produce a symmetric state space model for the flap control system.

D. US3D High Fidelity Aerothermal Simulation Setup

High fidelity CFD simulations were performed to characterize flow fields and to provide insight into any additional flow features not captured by the inviscid Euler equations. As a commercial CFD tool, US3D[13] was employed to solve a set of Navier-Stokes equations for a half-body geometry of the entry vehicle with a symmetry plane. The half-body of Pterodactyl and the coordinate system used in CFD are shown in Figure 9.

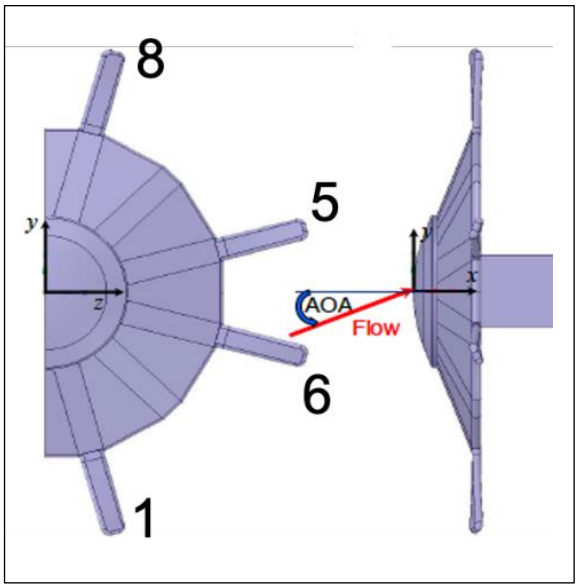

Figure 9 Pterodactyl coordinate system used in US3D

The coordinate origin is located at the tip of the cap. The *x* axis is aligned with the streamwise direction, the *y* axis is in the vertical direction from the coordinate origin, and the *z* axis points towards the spanwise direction normal to the symmetry plane following the right-hand rule. Note that the flap geometry is different than that shown in Figure 5. This decision was made to develop an understanding of what happens at the flap/rib connection and highlight the effects of a twisted flap. Twisted flaps were considered because in this iterative design process they are a mechanism to provide increased control authority in the event additional roll compensation is needed. More details on roll compensation can be found in reference 14.

The flight condition for this US3D run was at an altitude of 71 km from sea level, a Mach number of 31, and an angle of attack of -13 degrees. The corresponding pressure, temperature, and the sonic velocities were 4.48 Pa, 216.84 K, and 295.2 m/s, respectively. The Reynolds number based on the diameter without fins (2.816m) is 1.30×10^5. Three structured computational grid sets depending on the spatial resolution, i.e., coarse, medium, and fine computational meshes, were generated for US3D simulations. The number of grid cells were approximately 8, 20, and 73 million, respectively, as shown in Figure 10. Ivy Bridge or Haswell CPUs in a range of 1,200 to 1,800 were employed for US3D simulations in NAS cluster. The simulation time per 100,000 iterations for 8, 20, and 73 million grid systems using 1200 CPUs are about 27, 55, and 145 hours, respectively. More than one million iterations were executed to obtain an iterative converged solution for coarse and medium grid systems.

The coarse grid set was used to obtain a converged solution which was interpolated onto the medium grid set for the final solution with sufficient spatial resolution. The first grid heights from the wall were 1 micrometer for the coarse and medium grids and 10 nanometers for the fine grids, and the corresponding wall units (y+) are less than 1.0. The flow around the vehicle was considered as an unsteady laminar viscous flow based on the altitude. A real gas model was employed within the CFD simulation and consists of 11 species of N_2, O_2, NO, NO+, N_2+, O_2+, N, O, N+, O+, and e with finite rate chemistry. The second-order implicit Euler time integration with line relaxation was applied, and vibration-electronic energy was enabled for the final solution. The radiative equilibrium with emissivity of 0.85 was imposed on the walls.

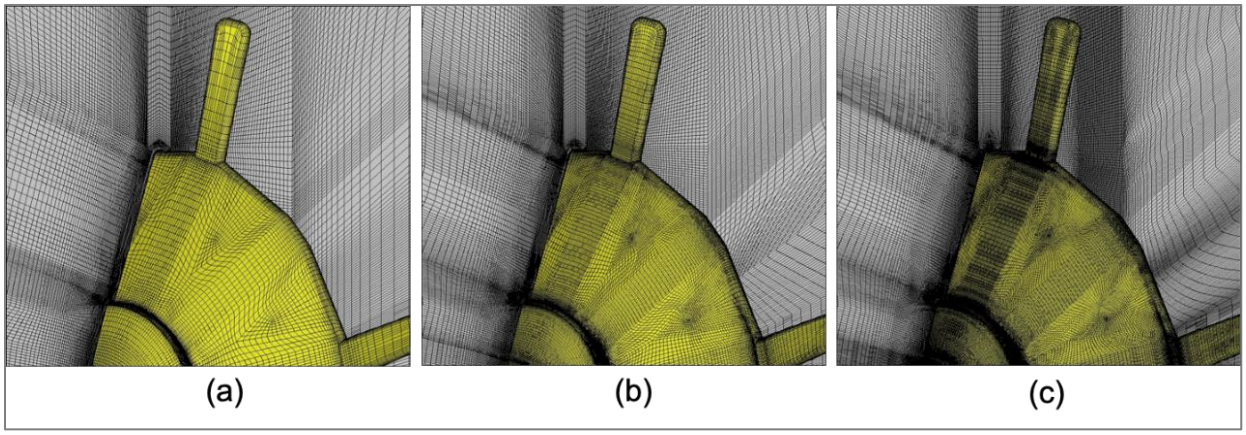

Figure 10 Computational grid sets: (a) Coarse grids with 8 million cells, (b) Medium grids with 20 million cells, (c) Fine grids with 73 million cells

IV. Cart3D Aerodynamic Results

Each Cart3D case was monitored for convergence by ensuring that the aerodynamic forces reached steady state. The final aerodynamic database consists of a total of 3,402 separate data points after using the symmetry process based on 1,050 Cart3D runs. The following sub-sections discuss the behaviors and trends found from the Cart3D analysis.

A. Aft Section Flow Features

The exposure of the payload in the aft section of the vehicle illustrates interesting flow features that can affect future Pterodactyl vehicle designs. For small angles of attack and sideslip, the flow around the payload typically has a low Mach number and temperature. However, at more extreme attitudes, regions of high-speed flow were observed around the payload at supersonic and hypersonic speeds. Figure 11 shows the pressure contours of two different flight configurations that display high Mach numbers aft of the heatshield that could negatively impact the payload. Although Cart3D is an inviscid solver and cannot model the viscous nature of wake flow, the indication of flow expanding around the heatshield highlights the importance of studying the wake flow with a fully viscous Navier-Stokes solver.

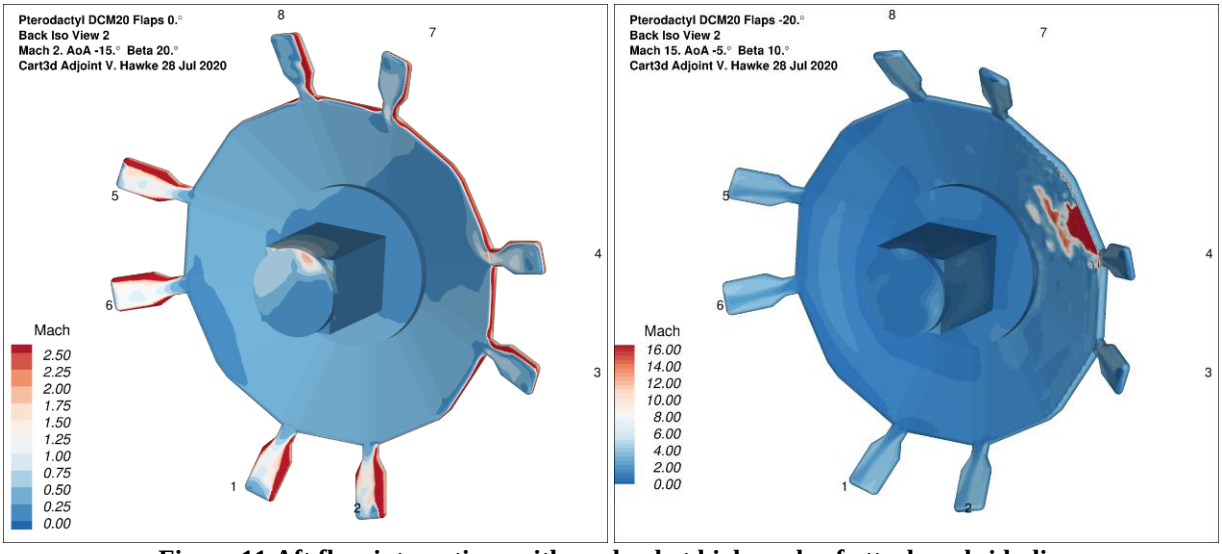

Figure 11 Aft flow interactions with payload at high angle of attack and sideslip

B. Vehicle Component Force and Moment Characteristics

The primary data products from Cart3D are the force and moment coefficients produced. This provides an understanding of the aerodynamic characteristics of the aeroshell and the flaps. Since Cart3D was run such that the aeroshell and each flap was treated as a separate component, an understanding of the contributions from each component can be examined. For brevity, the results of a single Mach number of 15 for a single geometry, where all the flaps are deflected 20 degrees into the flow, are plotted and are representative of the overall behavior. In Figure 12-14, the drag (C_D), side (C_S), and lift (C_L) force coefficients are plotted and each line on the plot corresponds to different sideslip conditions. As expected, C_D demonstrates parabolic behavior and the magnitude of C_D for the negative and positive values of equivalent sideslip match. Also, as the sideslip angle increases in magnitude, the amount of C_D decreases, which is due to the reduction of surface area facing the flow. The side force coefficient, as expected, increases at non-zero sideslip and the lift force coefficient increases as angle of attack increases.

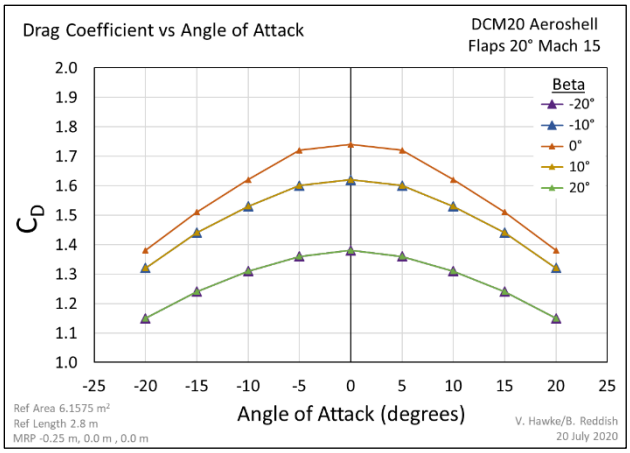

Figure 12 Drag force coefficient for aeroshell at Mach 15 and flap deflection angle of 20°

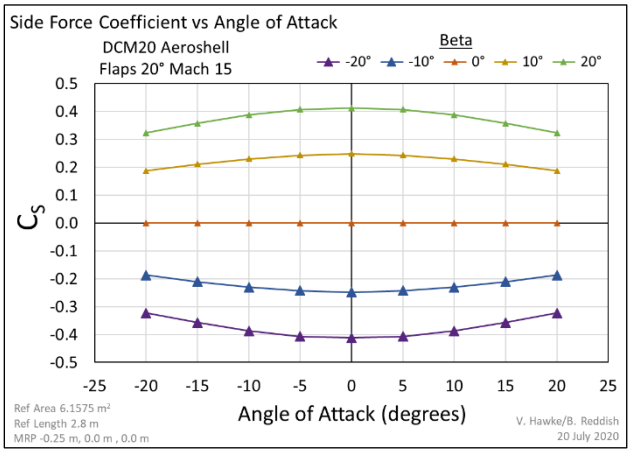

Figure 13 Side force coefficient for aeroshell at Mach 15 and flap deflection angle of 20°

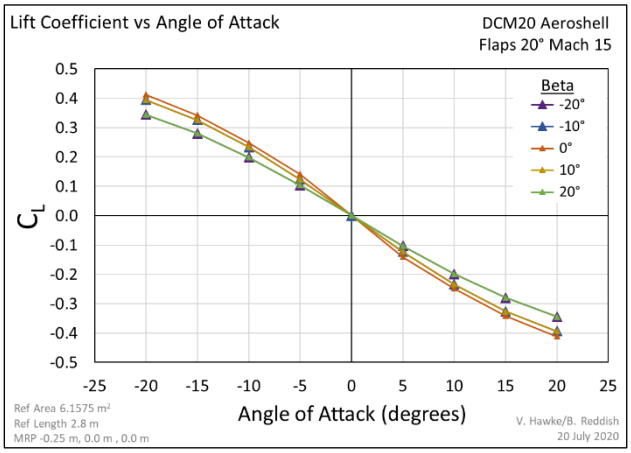

Figure 14 Lift force coefficient for aeroshell at Mach 15 and flap deflection angle of 20°

In Figure 15 - 17, the rolling (C_{MX}), pitching (C_{MY}), and yawing (C_{MZ}) moment coefficients are plotted and each line on the plot corresponds to different sideslip conditions. As expected with the symmetrization and zeroing of the rolling moments (pairs of flaps negate each other throughout the full range) the rolling moment (about *x*) shows zero values. Also as expected, the yawing moment (about *z*) coefficient increases with increasing sideslip angle and the pitching moment (about *y*) coefficient increases as angle of attack increases.

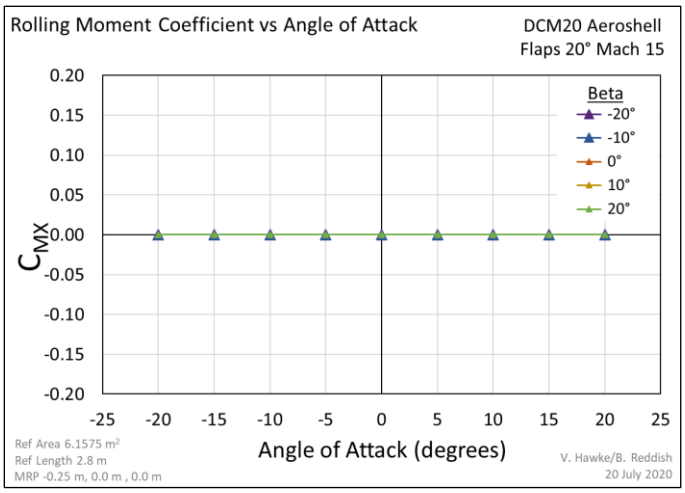

Figure 15 Rolling moment coefficient for aeroshell at Mach 15 and flap deflection angle of 20°

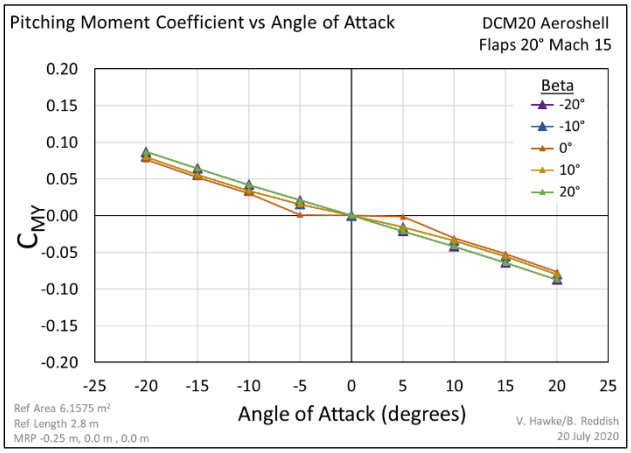

Figure 16 Pitching moment coefficient for aeroshell at Mach 15 and flap deflection angle of 20°

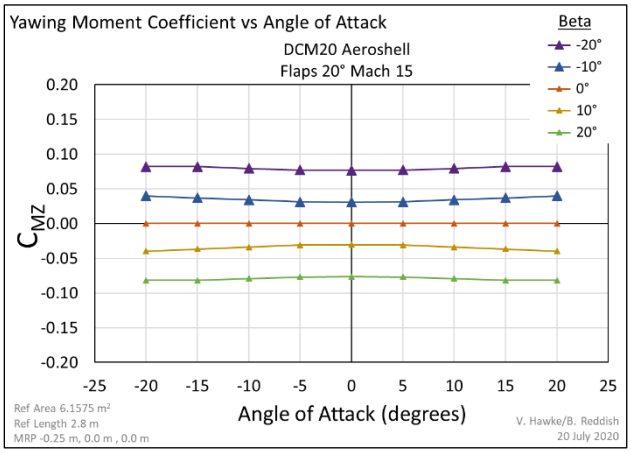

Figure 17 Yawing moment coefficient of aeroshell at Mach 15 and flap deflection angle of 20°

In Figure 18 - 23, the same force and moment coefficients are plotted for the flaps at Mach 15, a sideslip of zero, and a flap deflection angle of 20 degrees into the flow. Each line in the plot corresponds to a particular flap. The first aspect to note is that the magnitude of the force coefficients for the flaps are one to two orders of magnitude less than that of the aeroshell. This implies that the dynamics of the vehicle will be dominated by the aeroshell, but this does not imply that the flaps do not have the control authority to affect an attitude change in the vehicle. Okolo et al,[15] assess the controllability of the flaps in a separate paper.

The drag force coefficients for each flap will be additive to the total C_D. In Figure 18, it is shown that the added drag effect on the vehicle is relatively constant at $\alpha \leq 5$ deg, but the change in C_D as α increases from 5 deg is more dramatic. As expected, the lift force coefficient increases for α less than zero and decreases for α greater than zero. Most notable is the presence of a non-zero magnitude of side force. Although this is a small number, it is not insignificant and shows that the placement of the flaps, off the primary axes, generates a side force that can be used to change attitude of the vehicle. The effect of flap placement is further demonstrated in the plots of moment coefficient.

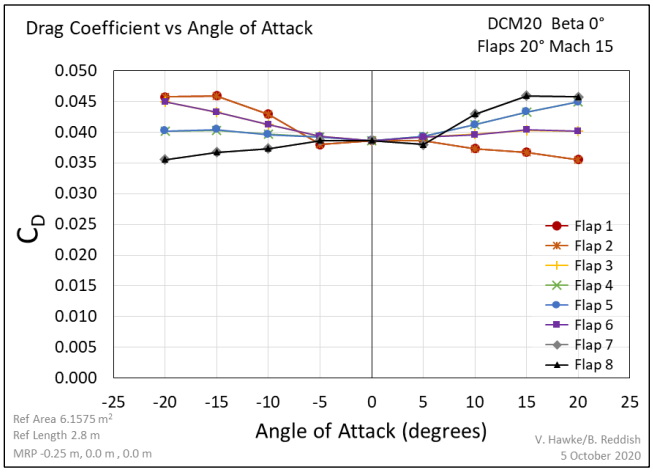

Figure 18 Drag force coefficient for flaps at Mach 15, β = 0°, and flap deflection angle of 20°

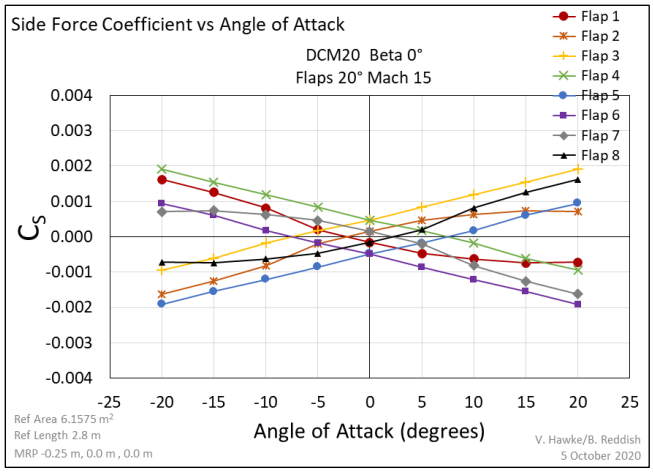

Figure 19 Side force coefficient for flaps at Mach 15, β = 0°, and flap deflection angle of 20°

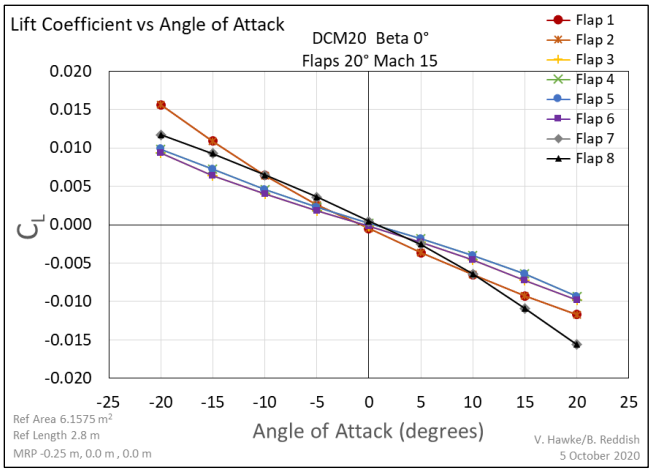

Figure 20 Lift force coefficient for flaps at Mach 15, β = 0°, and flap deflection angle of 20°

Recall that the flaps designated primarily for effecting a change in pitch (or angle of attack) are flaps 1, 2, 7, and 8 while the flaps designated primarily for effecting a change in yaw (or sideslip) are flaps 3 through 6. In Figure 21Figure 21, as expected, the pitching moment coefficient plot shows that the primary pitch flaps 1, 2, 7, and 8 effect a non-zero contribution to C_{MY}, but because of the off axis flap placement, flaps 3 through 6 also provide a non-zero C_{MY} contribution although it is smaller. The same phenomenon is found for yaw (Figure 22), flaps 3 through 6 provides a non-zero contribution to the yawing moment, but because of the off axis flap placement, flaps 1, 2, 7, and 8 also provide a non-zero C_{MZ} contribution although it is smaller. Finally, and most interestingly, the behavior of the rolling moment coefficient (Figure 23) further demonstrates the coupled effect on the moment from flap placement. The C_{MX} contribution from all flaps is non-zero and the contribution from flaps 3 through 6 provide larger contributions as compared to flaps 1, 2, 7, and 8. This indicates that the control system will have access to multiple combinations of flaps to affect a wide variety of attitude changes.

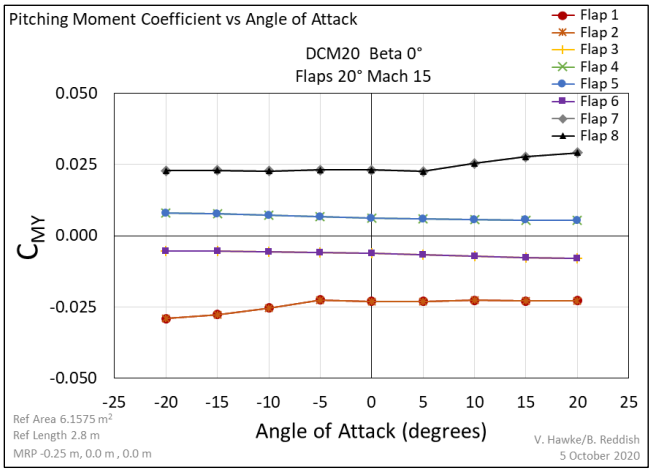

Figure 21 Pitching moment coefficient for flaps at Mach 15, β = 0°, and flap deflection angle of 20°

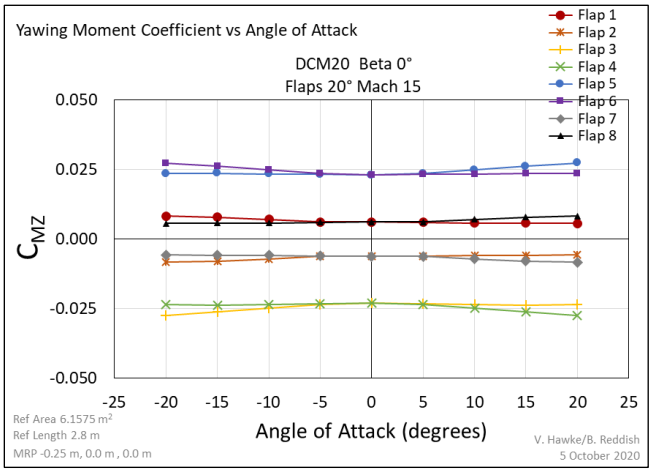

Figure 22 Yawing moment coefficient for flaps at Mach 15, β = 0°, and flap deflection angle of 20°

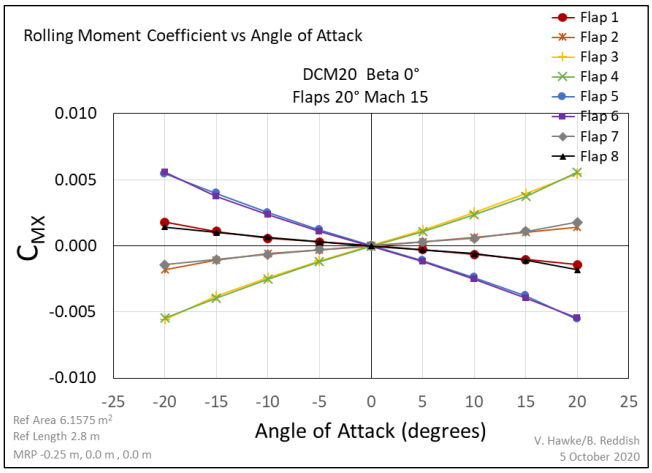

Figure 23 Rolling moment coefficient for flaps at Mach 15, β = 0°, and flap deflection angle of 20°

In taking a deeper look at how the side force and rolling moment coefficient change as the sideslip angle is increased, it was found that the overall magnitude of the side force increases with sideslip angle. This implies that the ability to affect side force is increased at non-zero sideslip (Figure 24). Additionally, an interesting trend in the rolling moment coefficient emerges (Figure 25). For all flaps at zero sideslip and zero angle of attack, C_{MX} is zero, and at non-zero α the C_{MX} contribution cancels out when each pair of pitch flaps and yaw flaps are deflected together. But at non-zero sideslip angles it is demonstrated that deflecting flaps 1, 2, 7, and 8 simultaneously imparts a very small non-zero C_{MX} for a given angle of attack and when these flaps are deployed independently, a larger C_{MX} value is imparted. For flaps 3 through 6 it is found that for a sideslip of 10° and an α of -2.7°, C_{MX} for flap 4 and flap 6 equals zero, while flaps 3 and 5 must be deflected simultaneously to further zero out C_{MX} (vice versa at α of 2.7°). This side force and rolling moment behavior show the strongly coupled behavior of the flaps.

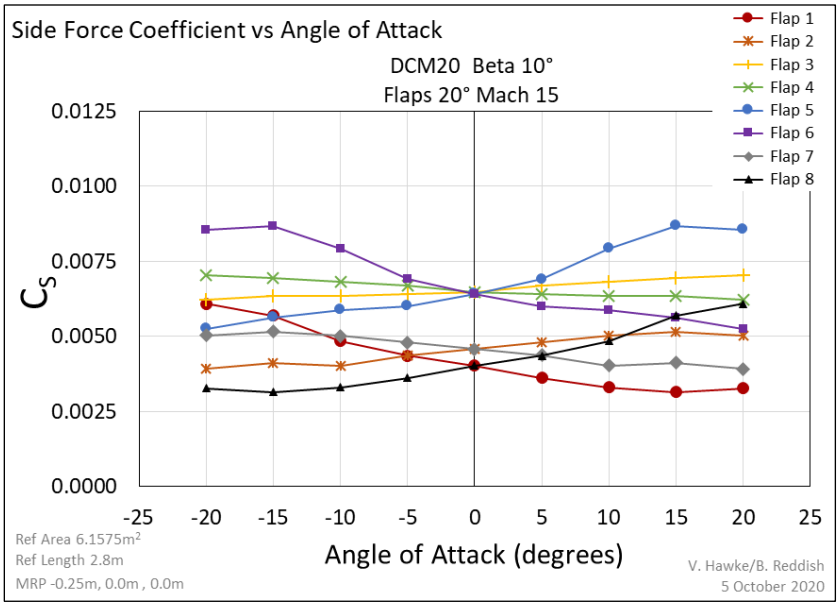

Figure 24 Side force coefficient for flaps at Mach 15, β = 10°, and flap deflection angle of 20°

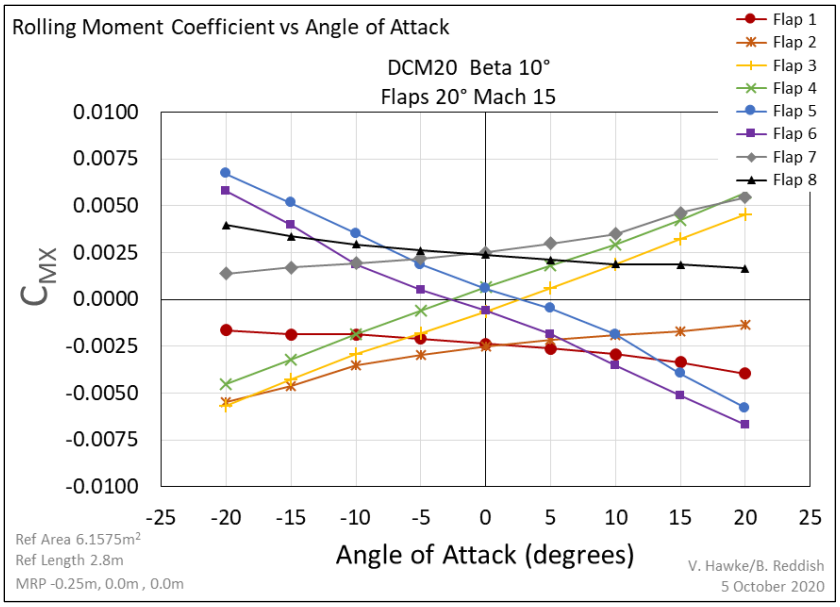

Figure 25 Rolling moment coefficient for flaps at Mach 15, β = 10°, and flap deflection angle of 20°

C. Trim Analysis

To further conceptualize the control capability of the flaps when combined with the aeroshell, a trim analysis was conducted based on the moments produced by certain pairs of flaps. A pitch up configuration is defined as having the two leading edge flaps fully deflected at 30° and the rest of the flaps retracted out of the flow at -45°. Conversely, the pitch down configuration is defined as the trailing edge flap fully deflected at 30° with the remaining flaps at -45°. A depiction of these two flight configurations and resulting trim angle of attack and L/D are shown in Figure 26. The maximum alpha trim value for the fully deflected flaps was 13° which is within the limitations to keep the center of pressure on the nose cap. The highest trim value was observed at Mach 10, and drops off rapidly for lower Mach numbers. A yaw trim analysis was conducted in a similar manner as shown in Figure 27. Because of the vehicle symmetry, the yaw capabilities match that of the pitching capabilities in terms of trim values. The L/D profile of the yaw trim plots show a greater reduction of L/D at higher Mach numbers at an angle of attack of 10°.

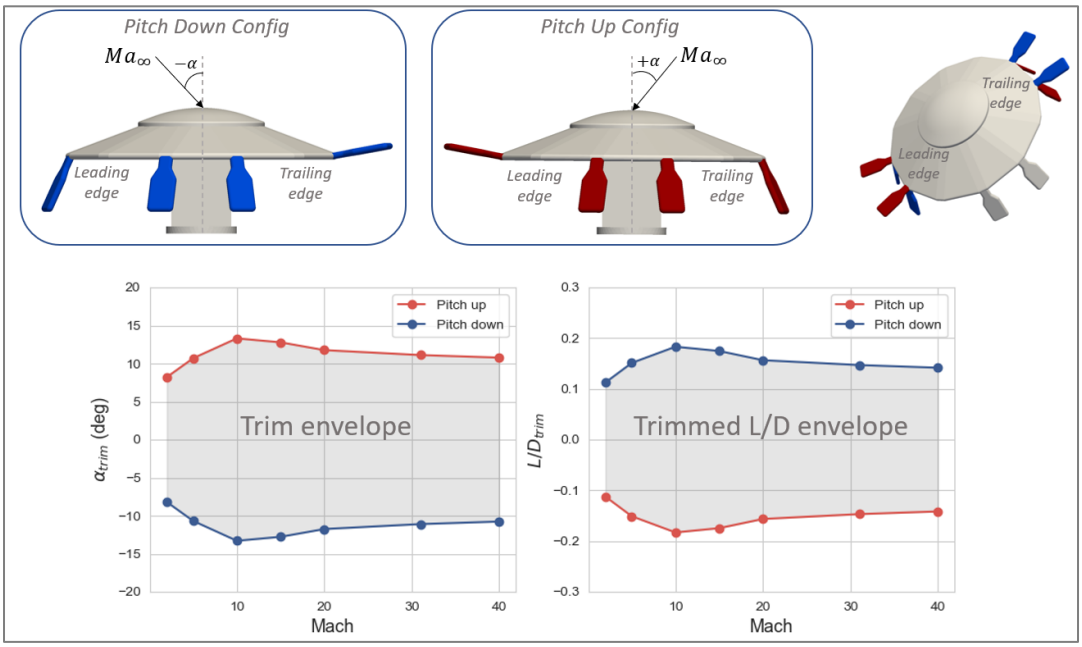

Figure 26 Pitch up and pitch down trim conditions and corresponding L/D

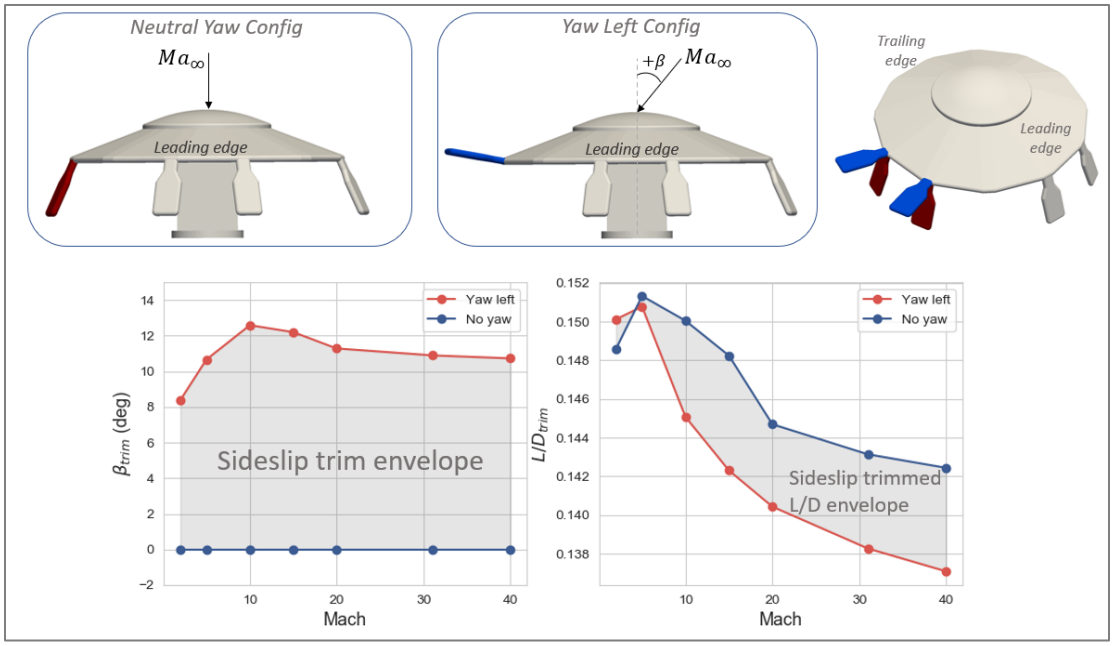

Figure 27 Yaw trim conditions and corresponding L/D at $\alpha = 10°$

The variation in angle of attack for trimmed configurations showed that the pitch flaps at 20° resulted in a greater trim value than the pitch flaps at 30° for high hypersonic Mach numbers. This result is shown in Figure 28, where after a Mach number of 15, the flaps deflected at 20° produce a trim angle of attack that is about 1 degree higher than the 30° flaps. This result suggests, that for a 70° sphere-cone forebody, a higher deflection of pitch flaps does not directly correlate with a higher angle of attack. This observation sets a limitation on the maximum effective flap deflection angle. In terms of sensitivity, the influence of flap deflection is high in the range of 0° to 10° flap deflection for Mach numbers of 20 and greater. The ability to deflect a flap past 10° becomes more important for high angles of attack at Mach numbers less than 20.

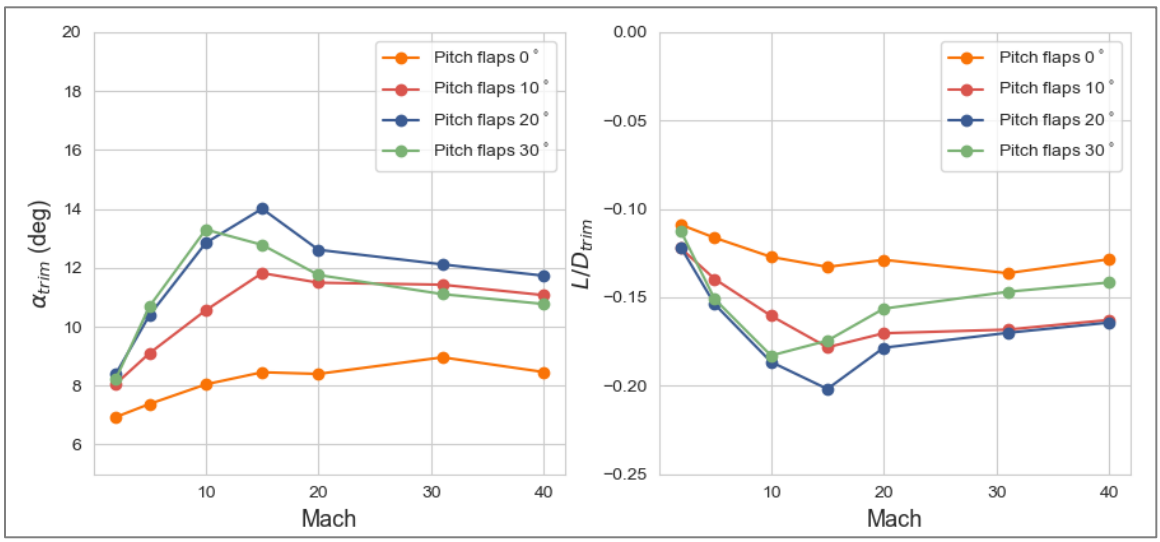

Figure 28 Pitch trim conditions for different flap deflection angles

The resulting aerodynamic database and Cart3D runs were passed to the Controls and Aerothermal/TPS Design teams to complete stability and control analysis for the vehicle/control system configuration and aeroheating environments for TPS modeling of the flaps.

V. US3D Aerothermodynamic Results

The following results for an unsteady US3D (see solver information in above section on US3D setup) simulation at Mach 31 and α = -13° are fully converged, with sufficient spatial resolution from the medium resolution grids illustrated in Figure 10b. The residual dropped from 10^7 to 130 over more than million iterations. The Mach number (Mach), pressure (p), translational temperature (*t*), and vibrational temperature (*tv*) distributions on the symmetry plane are shown in Figure 29. The shock standoff distance at the centerline is 94 mm from the wall and after the shock, the pressure and temperature increase, while the Mach number decreases. Due to the negative angle of attack of -13°, much larger pressure levels are found near the upper body compared to the lower body. Just behind the shock, the translational temperature increases up to 17800 K, and sharply decreases to 10000 K because some energy is transferred to the dissociations and ionizations in chemical reactions and the increase of the vibrational energy. Streamlines with vectors and Mach number contours on the symmetry plane behind the entry vehicle are shown in Figure 30. The flow turns around the shoulder of the skirt and eventually a flow separation occurs behind the shoulder. Large-scale primary recirculation structures exist behind the rear skirt.

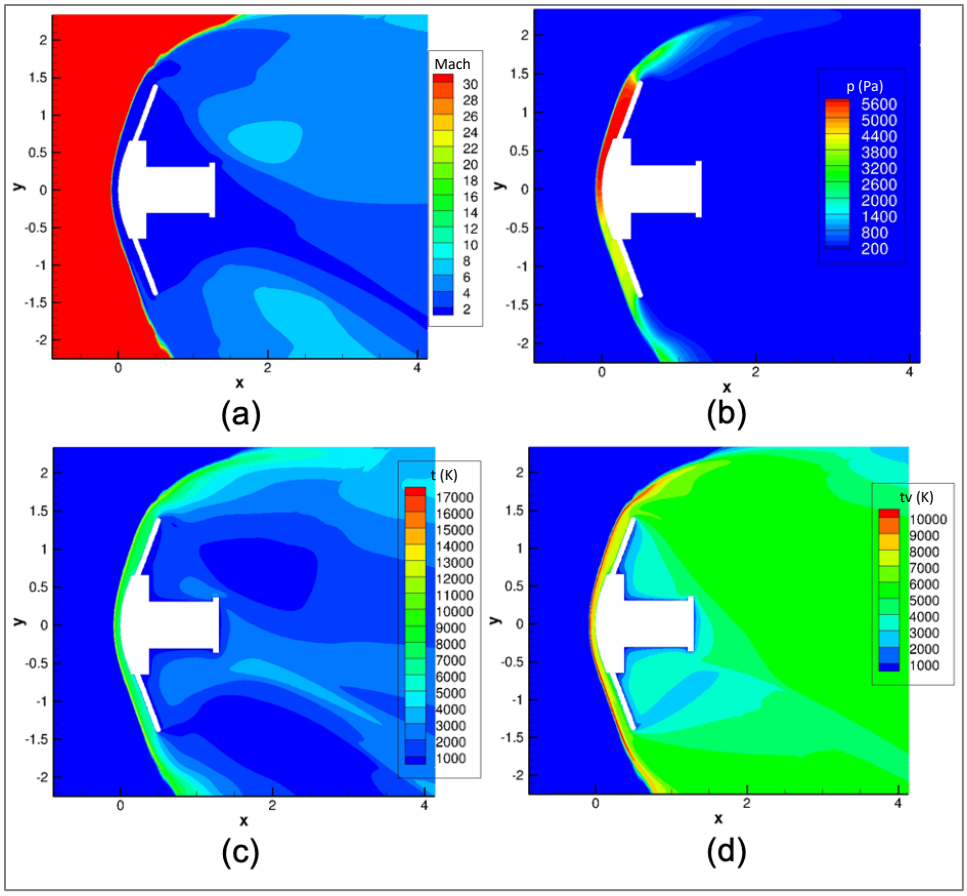

Figure 29 Symmetry plane, contour plots of:
(a) Mach number, (b) pressure (Pa), (c) translational temperature (K), and (d) tv vibrational temperature (K) from finite-rate real-gas simulation with US3D Freestream Mach number 31, α -13°, and Rn 1.30×10^5

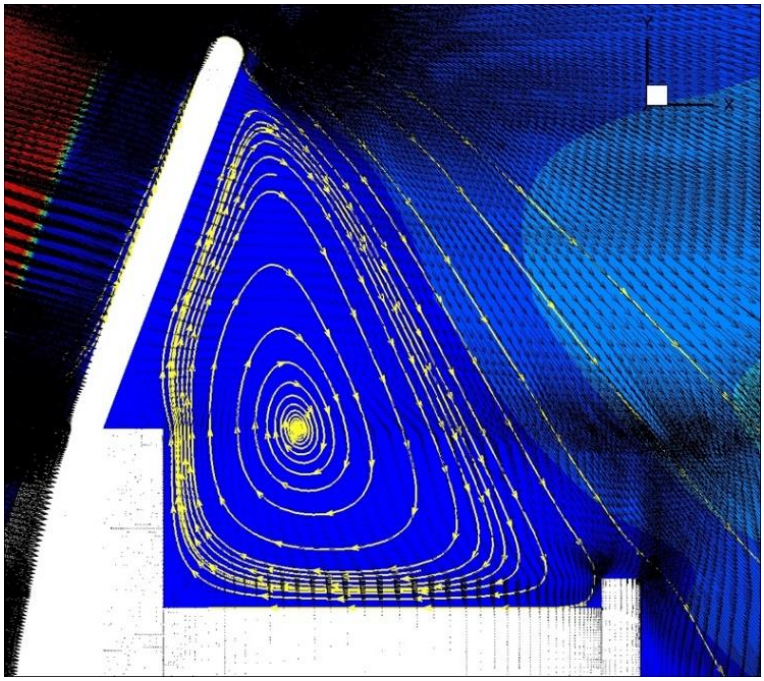

Figure 30 Streamlines with vectors and Mach number contours on symmetry plane

In order to size the TPS on the aeroshell and flaps, the surface quantities including pressure (p), temperature (t), heat flux (Q_w), and shear stress (τ_w) are investigated in detail. For better understanding, the half-body is mirror copied with respect to the symmetry plane.

Figure 31 shows the pressure distributions on the windward and aft surfaces, respectively. Given the negative angle of attack of the vehicle, larger pressure levels develop on the windward side of the flap as compared to that on cap and front. Among all flaps, the maximum pressure of 9704 Pa occurs on flaps 1 and 2. The recovered pressure on the aft surfaces become larger on side flaps 3, 4, 5 and 6 compared to the vertical flaps 1, 2, 7 and 8 close to the symmetry plane where the angle of attack is defined. The pressure on the aft skirt is lower than the far field pressure of 4.48 Pa, because the aft skirt is submerged in the wake region.

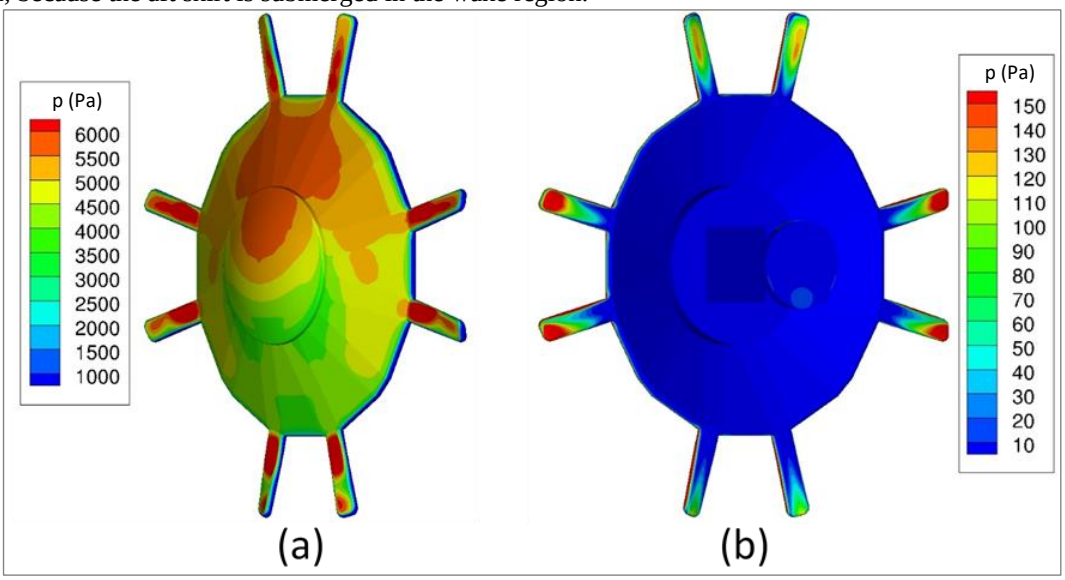

Figure 31 Pressure distribution on the: (a) windward surfaces, (b) aft surfaces

Figure 32 represents the temperature distributions on windward and aft surfaces. There is close correlation between the high surface temperature and pressure areas, i.e., high surface temperature areas on all flaps correspond to the high surface pressure areas in Figure 31. The maximum temperature location occurs at the front top corners of flaps 7 and 8. On each flap, the temperature on the windward edge is relatively larger.

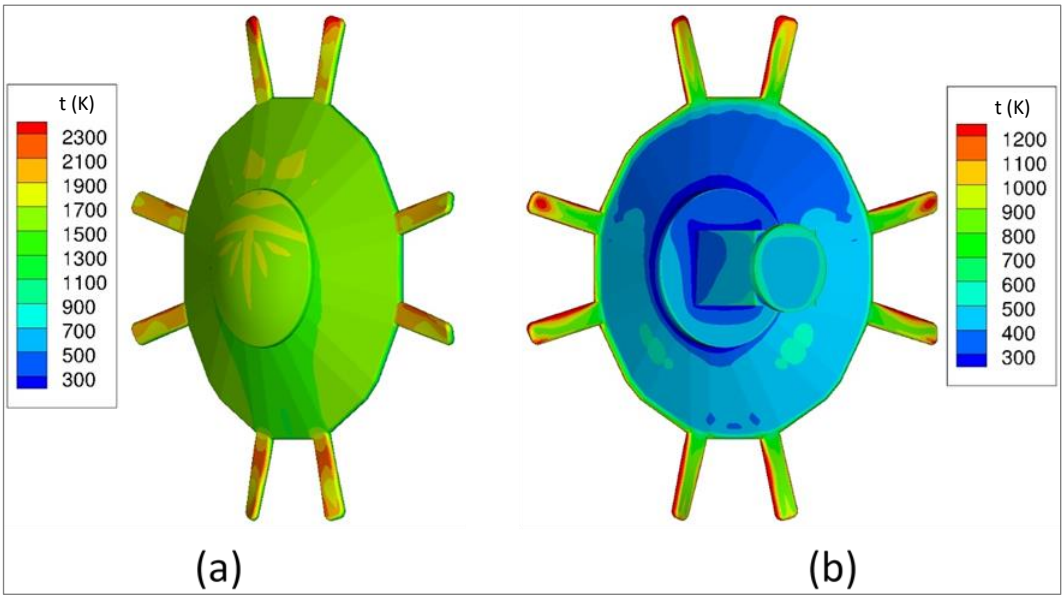

Figure 32 Temperature distribution: (a) windward surfaces and (b) aft surfaces

The surface heat flux distributions on the windward and aft surfaces shown in Figure 33 are highly correlated with the temperature distributions. Thus, the maximum heat flux of 3.88×10^6 W/m^2 is at the front top corners of flaps 7 and 8, which is consistent with the maximum temperature location. In addition, the erosion distributions will be consistent with the heat flux distributions. Therefore, it can be expected that the severe erosion locations will be at the front top corners of flaps 7 and 8, the upper front edges of flaps 3 and 6, the large pressure locations on flaps 1 and 2, and the upper front edges of flaps 4 and 5.

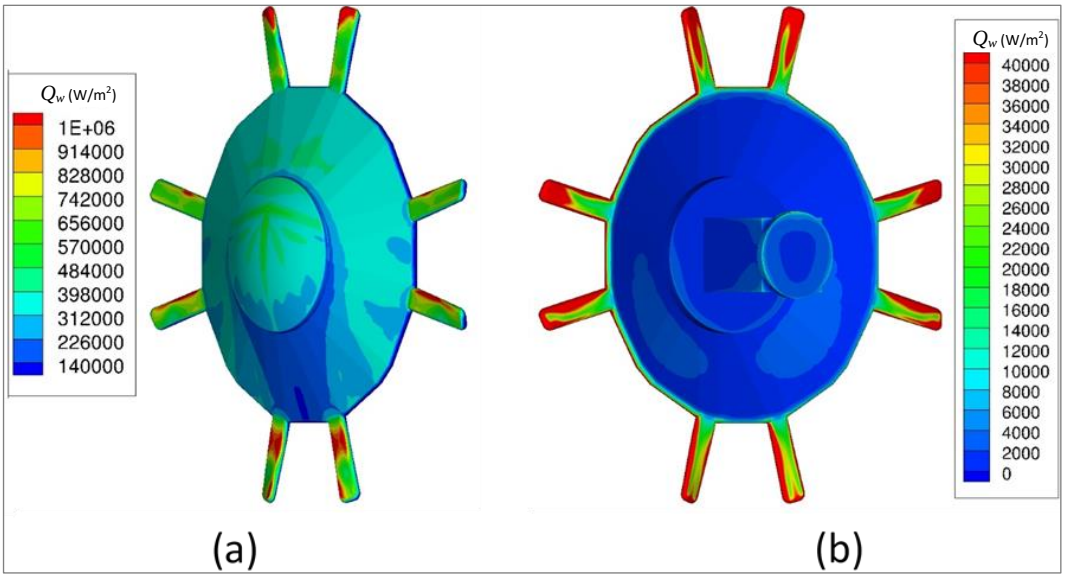

Figure 33 Heat flux distribution: (a) windward surfaces and (b) aft surfaces

In order to understand the maximum heat flux location, the wall shear pressure distribution on the windward and aft surfaces are further investigated as shown in Figure 34. The wall shear distribution is somehow inversely correlated with the pressure distribution. The large wall-shear-stress areas are mostly the front edges of the flaps and front shoulders of the skirt, while the high-pressure areas are on the windward surfaces of the flaps. The peak of the wall shear stress is 454 Pa and occurs at the top edges of Flaps 7 and 8, close to the maximum heat flux location. This implies that the wall shear stress significantly contributes to the maximum heat flux.

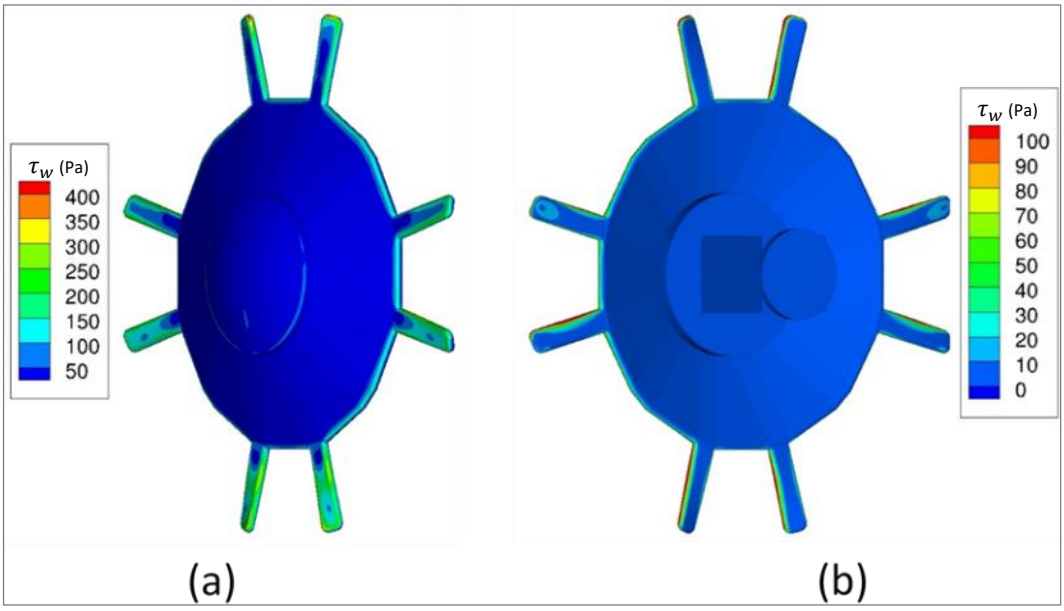

Figure 34 Wall shear stress distribution: (a) windward surfaces and (b) aft surfaces

Quantitative maximum values of each quantity on each surface of the part are documented in Table 3. Bold numbers represent the maximum. The maximum pressure is at flap 1, while the other maxima of temperature, heat flux, and wall shear stress occur at flap 8. Overall, the maximum values on the aft surfaces are smaller as compared to the values on the windward surfaces. The order of the maximum pressure level is $P_{Flap1} > P_{Flap6} > P_{Flap5} > P_{Flap8}$. The order of the maximum temperature or heat flux level is $T_{Flap8} > T_{Flap6} > T_{Flap1} > T_{Flap5}$ or $Q_{Flap8} > Q_{Flap6} > Q_{Flap1} > Q_{Flap5}$, which verifies the strong correlations between the surface temperature and heat. Interestingly, flap 1 with the maximum surface pressure is in third place in the maximum heat flux or temperature magnitudes. Also, the maximum heat flux on flap 8 is about 3 times larger than the maximum heat fluxes on the other flaps. The maximum wall shear stress occurs at flap 8, which indicates the significant contribution of wall shear stress and pressure play in the surface heat flux.

Table 3 Maximum quantity value in each part

Part	p (Pa)	t (K)	Q_w (W/m^2)	τ_w (Pa)	$\lvert\tau_{wx}\rvert$ (Pa)	$\lvert\tau_{wy}\rvert$ (Pa)	$\lvert\tau_{wz}\rvert$ (Pa)
Cap	5905	1880	6.0262E5	99	40	73	81
Front Skirt	5870	1851	5.6638E5	187	135	139	145
Flap 8 (& 7)	6378	**2994**	**3.8752E6**	**454**	**394**	**296**	**310**
Flap 5 (& 4)	7417	2214	1.1583E6	257	236	178	227
Flap 6 (& 3)	8126	2304	1.3587E6	296	242	218	255
Flap 1 (& 2)	**9704**	2258	1.2531E6	342	210	341	215
Rear Wall	554	1314	1.4356E5	104	103	28	30
Rear Structure	20	786	1.8365E4	5	4	5	3
Rear Disk	33	925	3.5330E4	12	12	8	4

VI. Conclusion

In this paper, a combination of medium and high-fidelity CFD analysis tools were used for the analysis of the aerodynamics and aerothermodynamics for a symmetric, mechanical DEV with a flap control system. The aerothermal analysis revealed that the combination of pressure and wall shear stress play an important role in the surface heat flux. The analysis of the vehicle aerodynamics demonstrated that, for a 70° sphere-cone forebody, a higher deflection of pitch flaps does not directly correlate with a higher angle of attack, setting a limitation on the maximum effective flap deflection angle. Additionally, due to the placement of the flaps in off-axis positions, the control system provides multiple combinations of flaps to affect a wide variety of attitude changes. However, a control and stability analysis is needed to further identify the control envelope and the resulting dynamics of this coupled behavior. Using this finding and the resulting data from these analyses, the objectives of this paper were met. First, the inherent aerodynamics of the vehicle with a flap control system were fully defined. Second, an aerodynamics database was successfully developed for stability and control analysis. Finally, a high-fidelity aerothermal analysis at conditions corresponding to high dynamic pressures provided key insights into the aeroheating environment and its impact on the flaps TPS modeling and sizing. Meeting these objectives brings the Pterodactyl project closer to establishing multiple, feasible G&C solutions for a DEV and realizing vehicles that can meet the promise of DEVs to deliver science payloads with a stowed diameter 3-4 times smaller than an equivalent rigid aeroshell.

VII. Future Work: CBAERO Aerothermal Analysis

CBAero was chosen for the aerothermal analysis because it provides results that can be anchored to the Cart3D solutions. This reduces the number of required high-fidelity results needed to define the aeroheating environment. Additionally, a vehicle TPS sizing program (TPSSizer) is designed to work directly with CBAero. In Hays et al.[16], this method was documented for the flap TPS design for a previous iteration. For this research, CBAero used the same mesh as used for Cart3D without the payload located in the aft region of the vehicle. As CBAero is Newtonian in nature the inclusion of the payload was deemed irrelevant. Removing this feature reduces the total number of mesh elements to solve which further reduces the computational time necessary to create the aerothermal database. Cart3D and CBAero both use a triangular surface mesh on the vehicle. The CBAero aerothermal anchoring feature creates a 4-dimensional unstructured tetrahedral mesh for both the high-fidelity CFD and the CBAero vehicle data to create non-dimensional correction factors that are applied to the CBAero data. Correction factors are created for boundary layer edge pressure, temperature, density, speed of sound, velocity, boundary layer thickness, momentum thickness, surface density, skin friction, convective heating, and radiative heating. The TPS modeling software utilizes the

anchored values of the CBAero database as the thermal input during different stages of flight. Once this analysis is complete an estimate of the TPS thickness can be made for the flaps.

VIII. Acknowledgments

The authors would like to thank NASA Space Technology Mission Directorate's Early Career Initiative (ECI) program for providing the resources to fund this work. Insights from colleagues across NASA were crucial in the success of this work, including Ashley Korzun, Michael Aftosmis, John Melton, Ryan McDaniel, and Khalil Bensassi. In addition, we would like to thank John O'Neil and Kenneth Hibbard of the John Hopkins University Applied Physics Laboratory for their insights and contributions to the aerothermal simulations. This work would not have been possible without the use of the NASA Advanced Supercomputing Facility (NAS) at NASA Ames Research Center. The authors thank the NAS for their support.

IX. References

1. Cassell, A. M., Smith, B. P., Wercinski, P. F., Ghassemieh, S. M., Hibbard, K. E., Nelessen, A. P., & Cutts, J. A. (2018). ADEPT, A Mechanically Deployable Re-Entry Vehicle System, Enabling Interplanetary CubeSat and Small Satellite Missions. *32nd Annual AIAA/USU Conference on Small Satellites.*

2. Steinfeldt, B. A., Theisinger, J. E., Korzun, A. M., Clark, I. G., Grant, M. J., & Braun, R. D. (2009). High Mass Mars Entry, Descent, and Landing Architecture Assessment. *AIAA Space 2009 Conference & Exposition*, (p. 3).

3. Dutta, S., & Green, J. S. (2019). Flight Mechanics Modeling and Post-Flight Analysis of ADEPT SR-1. *AIAA Aviation Forum* .

4. Sarigul-Klijn, N. (2014). Survey of planetary entry guidance algorithms. *Progress in Aerospace Sciences, 68*, pp. 64-74.

5. Alunni, A. I., D'Souza, S. N., Yount, B. C., Okolo, W. A., Margolis, B. W., Nikaido, B. E., Hays, Z. B. (2020). Pterodactyl: Trade Study for an Integrated Control System Design of a Mechanically Deployable Entry Vehicle. *AIAA SciTech Forum.* Orlando: AIAA.

6. Nikaido, B. E., D'Souza, S. N., Hays, Z. B., & Reddish, B. J. (2020). Pterodactyl: Aerodynamic and Aeroheating Database Development for Integrated Control Design of a Mechanically Deployed Entry Vehicle. *AIAA SciTech Forum.*

7. Kinney, D. J. (2004). Aero-thermodynamics for Conceptual Design. *42nd AIAA Aerospace Sciences Meeting and Exhibit.* Reno, Nevada.

8. Aftosmis, M. J. (2015). *Cart3D Documentation*. Retrieved July 2020, from https://www.nas.nasa.gov/publications/software/docs/cart3d/

9. Kinney, D. J., Garcia, J. A., & Huynh, L. (2006). Kinney, David, Joseph Garcia, and Loc Huynh. "Predicted convective and Radiative Aerothermodynamic Environments for Various Reentry Vehicles Using CBAERO. *4th AIAA Aerospace Sciences Meeting and Exhibit.* Reno, Nevada.

10. Aftosmis, M. J., Berger, M. J., & Melton, J. E. (1998). Robust and efficient cartesian mesh generation for component-based geometry. *AIAA Journal, 36*(6), 952-960.

11. Aftosmis, M., Berger, M., & Adomavicius, G. (2000). A parallel multilevel method for adaptively refines cartesian grids with embedded boundaries. *38th Aerospace Science Meeting and Exhibit*, 808.

12. Nemec, M., & Aftosmis, M. J. (2008). Adjoint-Based Adaptive Mesh Refinement for Complex Geometries. *46th AIAA Aeropsace Sciences Meeting.* Reno, Nevada.

13. Candler, G. V., Johnson, H. B., Nompelis, I., Subbareddy, P. K., Drayna, T. W., Gidzak, V. & Barnhardt, M. D. (2015). Development of the US3D Code for Advanced Compressible and Reacting Flow Simulations. *AIAA SciTech 2015*, Kissimmee, FL.

14. D'Souza, S. N., Alunni, A. I., Yount, B. C., Okolo, W. A., Margolis, B. W., Hibbard, K.E., Barton, J. D., Hawke, V., Hays, Z. B., and Reddish, B. J. (2021). Pterodactyl: System Analysis of an Asymmetric and Symmetric Deployable Entry Vehicle for Precision Targeting Using Flaps. *AIAA SciTech Forum.* Virtual: AIAA.

15. Okolo, W. A., Margolis, B. W., D'Souza, S. N., & Barton, J. D. (2020). Pterodactyl: Development and Comparison of Control Architectures for a Mechanically Deployed Entry Vehicle. *AIAA SciTech 2020 Forum.*

16. Hays, Z., Yount, B. Y., Nikaido, B. E., Tran, J., D'Souza, S. N., Kinney, D. J., & McGuire, M. K. (2020). Pterodactyl: Thermal Protection System for Integrated Control Deisgn of a Mechanically Deployed Entry *Vehicle. AIAA SciTech 2020*.